VLA and ATCA Search for Natal Star Clusters in Nearby Star-Forming Galaxies

Alan G. Aversa[1,2], Kelsey E. Johnson[3,4], and Crystal L. Brogan

National Radio Astronomy Observatory, 520 Edgemont Rd, Charlottesville, VA 22903

aaversa@nrao.edu

W.M. Goss

National Radio Astronomy Observatory, P.O. Box O, 1003 Lopezville Road, Socorro, NM 87801-0387

D.J. Pisano[5]

WVU Department of Physics, P.O. Box 6315, Morgantown, WV 26506

ABSTRACT

In order to investigate the relationship between the local environment and the properties of natal star clusters, we obtained radio observations of 25 star-forming galaxies within 20 Mpc using the Very Large Array (VLA) and the Australia Telescope Compact Array (ATCA). Natal star-forming regions can be identified by their characteristic thermal radio emission, which is manifest in their spectral index at centimeter wavelengths. The host galaxies in our sample were selected based upon their likelihood of harboring young star formation. In star-forming regions, the ionizing flux of massive embedded stars powers the dominant thermal free-free emission of those sources, resulting in a spectral index of $\alpha \gtrsim -0.2$ (where $S_\nu \propto \nu^\alpha$), which we compute. With the current sensitivity, we find that of the 25 galaxies in this sample only five have radio sources with spectral indices that are only consistent with a thermal origin; four have radio sources that are only consistent with a non-thermal origin; six have radio sources whose nature is ambiguous due to uncertainties in the spectral index; and sixteen have no detected radio sources. For those sources that appear to be dominated by thermal

---

[1]Steward Observatory, 933 N Cherry Ave., Tucson AZ 85721

[2]NSF Research Experiences for Undergraduates program

[3]Department of Astronomy, P.O. Box 400325, University of Virginia, Charlottesville, VA 22904-4325

[4]Adjunct astronomer at the National Radio Astronomy Observatory

[5]Adjunct assistant astronomer at the National Radio Astronomy Observatory, P.O. Box 2, Rt. 28/92, Green Bank, WV 24944-0002

emission, we infer the ionizing flux of the star clusters and the number of equivalent O7.5 V stars that are required to produce the observed radio flux densities. The most radio-luminous clusters that we detect have an equivalent of $\sim 7 \times 10^3$ O7.5 V stars, and the smallest only have an equivalent of $\sim 10^2$ O7.5 V stars; thus these star-forming regions span the range of large OB-associations to moderate "super star clusters" (SSCs). With the current detection limits, we also place upper limits on the masses of clusters that could have recently formed; for a number of galaxies we can conclusively rule out the presence of natal clusters significantly more massive than the Galactic star-forming region W49A ($\sim 5 \times 10^4$ M$_\odot$). The dearth of current massive cluster formation in these galaxies suggests that either their current star formation intensities have fallen to near or below that of the Milky Way and/or that the evolutionary state that gives rise to thermal radio emission is short-lived.

Subject headings: galaxies: star clusters—galaxies: irregular—galaxies: starburst—stars: formation—HII regions

1. Introduction

Most stars are born in clusters or associations of some kind (e.g. Lada & Lada 2003; de Wit et al. 2005). As a result, the clustered mode of star formation plays a fundamental role in understanding star formation in general. In the Galaxy, stars within a cluster can often be individually resolved, and thus detailed studies of the resolved structure and interplay between stars are possible. However, our Galaxy only presents a narrow range of environmental conditions, and we are compelled to study more distant objects in order to investigate the impact of different environments on star cluster formation.

In relatively nearby starburst galaxies ($\lesssim 20$ Mpc), recent star formation activity has typically been resolved in massive star clusters. The *Hubble Space Telescope* (*HST*) was instrumental in the discovery of the so-called "super star clusters" (SSCs), which have been detected in significant numbers (e.g. Whitmore 2002). Large samples of less massive clusters have also been detected, typically following a power-law distribution down to the completeness limits of the data. However, despite the large samples of high quality optical data, the impact of the local environment on massive star cluster formation is far from understood. One of the primary obstacles has been the very nature of star formation, which is obscured at optical wavelengths. Once clusters have emerged from their birth material to be observable in optical light, their birth environments can no longer directly be probed.

To study the dependence of environment on star formation, it is necessary to penetrate through the optically thick cocoon before the system has had time to evolve and disperse its gas and dust, which Kobulnicky & Johnson (1999) have estimated to last $\sim 15\%$ of the lifetimes of the embedded cluster's stars. To find evidence of natal clusters of massive stars, observations at wavelengths

$\gtrsim$ a few μm are necessary. High spatial resolution radio observations at centimeter wavelengths are a powerful way to identify the earliest phases of star-formation regions via their "inverted" spectral indices α, where $S_\nu \propto \nu^\alpha$ and $\alpha > -0.2$; this type of spectral energy distribution is similar to that of HII regions, which exist on a smaller scale around individual massive stars in our Galaxy, i.e., ultracompact HII regions (Wood & Churchwell 1989). If the larger ultra-dense HII regions (UDHIIs) associated with natal clusters of massive stars emit sufficient thermal bremsstrahlung radiation, we can detect the signature of this radiation by its radio signature.

High spatial resolution radio observations have revealed a sample of very young massive star clusters still embedded in their birth material in a number of galaxies, including: NGC 5253 (Turner, Ho, & Beck 1998), He 2-10 (Kobulnicky & Johnson 1999; Johnson & Kobulnicky 2003), NGC 2146 (Tarchi et al. 2000), NGC 4214 (Beck et al. 2000), Haro 3 (Johnson et al. 2004), NGC 4449 (Reines et al. 2008), and SBS 0335-052 (Johnson et al. 2009). These heavily enshrouded clusters contain hundreds to thousands of young massive stars; these nascent stars create compact HII regions within the dense environment and manifest themselves as optically thick free-free radio sources, some of which have been confirmed as luminous mid-infrared sources (Beck, Turner, & Gorjian 2001; Gorjian, Turner, & Beck 2001; Vacca, Johnson, & Conti 2002; Reines et al. 2008).

Perhaps not surprisingly, the most massive and luminous natal clusters were the first to be identified in nearby galaxies (as in the sample cited above). However, if star cluster formation tends to follow a power-law, as suggested by optical studies (Whitmore 2002), we should expect to find a continuum of extragalactic star clusters ranging from objects similar to individual Galactic UCHII regions to the massive proto-globular clusters common in starburst galaxies. Furthermore, current theory suggests that the properties of massive star clusters will largely be dependent on the pressure of their formation environment (Elmegreen & Efremov 1997). Therefore, the most vigorous starbursts host the most massive star clusters, while relatively quiescent galaxies (like our own Milky Way) will tend to contain only low mass clusters and associations. If we wish to understand how massive star cluster formation depends on the local environmental properties as well as to understand it in a statistical sense, we must fill in the continuum between galactic UCHIIs and natal SSCs with the aim of building a large sample. For this purpose, the observations presented here are part of an effort to increase the known sample of natal clusters in relatively nearby galaxies. We use the NRAO[1] Very Large Array (VLA) and the ATNF[2] Australia Telescope Compact Array (ATCA) to image 25 galaxies selected for their likelihood of containing natal star formation.

---

2. Observations

2.1. The Sample

This sample includes 25 galaxies that were selected for this study based on their distance and their likelihood of containing natal star formation. Indicators of possible natal star formation included either (1) membership in the Markarian UV catalog, the Arp catalog of irregular and tidally interacting galaxies, or the VV catalog of interacting galaxies (18 out of the 25 galaxies), or (2) evidence of Wolf-Rayet (W-R) features in the host galaxy's spectra (10 out of the 25 galaxies), necessitating the presence of young massive stars, or (3) identification of the galaxy as a blue compact dwarf (BCD), again an indicator of recent star formation (6 out of the 25 galaxies). Several of the galaxies in this sample fall into more than one of these three categories. Due to sensitivity and spatial resolution limitations, only galaxies within ∼20 Mpc were included. We give a brief overview of the selected galaxies in §A.1-A.2, and their characteristics are summarized in Table 1.

2.2. VLA and ATCA Observations

We observed the eight southern hemisphere galaxies in our sample on 2002 March in 3 cm (8.6 GHz) and 6 cm (4.8 GHz) bands with the Australia Telescope Compact Array (ATCA) in the 6A configuration. With the Very Large Array (VLA), we observed the 19 northern hemisphere galaxies on 2002 February 15 and 2002 October 21 using the A-configuration for 3.6 cm (8.5 GHz) and the C-configuration for 1.3 cm (22 GHz) observations.

For the ATCA data, we excluded visibilities with uv values < 10 kλ in the 6 cm band to better match the largest spatial scale to which the 3 cm observations are sensitive. We then imaged the ATCA 3 cm data with a robustness parameter of 3.0 (close to natural weighting), which helped to mitigate noise levels in that band, and imaged the 6 cm data with a robustness of 0.0 to add more weight to longer baselines, thereby increasing the spatial resolution of the resulting images. Finally, we matched the convolution kernel of the ATCA 3 cm images to that of the 6 cm images during the imaging process.

We followed a similar procedure to create images of the VLA data. Since the VLA was in the A-configuration for the 3.6 cm observations, the resulting images have higher spatial resolution than images made with 1.3 cm observations in the C-configuration. Consequently, we imaged the 1.3 cm data with a robustness parameter of 3.0 and excluded all visibilities < 12 kλ in the uv plane. This process approximately matches the largest spatial scale to which the data are sensitive. The 3.6 cm data were imaged with a robustness parameter of 0.0 in order to obtain slightly higher angular resolution than with natural weighting.

We created images of all ATCA and VLA data with the IMAGR task of the Astronomical Image Processing System (AIPS). The parameters for the imaging process are summarized in Table 2,

and the resulting radio contours for galaxies with detected emission are shown overlaid on optical or infrared images in Figures 1 to 9.

The nature of a radio source can be constrained using its spectral index α, where $S_\nu \propto \nu^\alpha$. Supernova remnants typically have radio spectral indices of $\lesssim -0.2$ (e.g. Green 1984; Weiler et al. 1986). Thermal sources (e.g. HII regions) can be identified by their signature thermal bremsstrahlung emission. Purely optically thin thermal emission has $\alpha \sim -0.1$, while in the optically thick limit the emission has $\alpha = +2$. The specific spectral morphology of an HII region at radio frequencies is due to a combination of size and density structure. The frequency at which thermal emission transitions from optically thick ($\alpha = +2$) to thin ($\alpha = -0.1$) is higher for denser HII regions.

In order to compute a spectral index

$$\alpha_{AB} = \frac{\log_{10}\left(F_A/F_B\right)}{\log_{10}\left(\nu_A/\nu_B\right)} \tag{1}$$

based on two flux densities F_A, F_B and frequencies ν_A, ν_B, it is important to match the spatial scales to which the different frequencies are sensitive in so far as possible. Given the nature of interferometers, it is virtually impossible to match the synthesized beams precisely, but steps can be taken to improve the extent to which the synthesized beams are compatible. To this end, when imaging the radio observations presented in this paper, we limited the uv coverage of each data set, we varied the weighting of longer and shorter baselines, and finally we convolved the frequencies to the same synthesized beam. (This final step does not compensate for any missing uv coverage; however, it is important to match the point response function.)

For the purposes of this paper, we consider a source to be dominated by thermal emission if it has a spectral index that is consistent with $\alpha > -0.2$ within 1σ uncertainty (Table 5). Likewise, we consider a source to be dominated by non-thermal emission if it has a spectral index that is consistent with $\alpha < -0.2$ given 1σ uncertainty. However, in many cases it is not possible to determine unambiguously whether a source is thermal, non-thermal, or a combination thereof for two main reasons: (1) several of the sources presented here are clearly extended and likely contain multiple components, and (2) the spectral indices have significant uncertainties, and many sources that nominally appear thermal could also be consistent (within uncertainty) with being non-thermal and *vice versa*; we classify these sources as "ambiguous."

3. Results

Of the 25 galaxies in this study, only five have radio sources that are dominated by thermal emission, four have sources that are dominated by non-thermal emission, six have radio sources that are ambiguous within the uncertainty limits, and sixteen have no detected radio sources (Figures 1 to 9; Tables 3 and 4). To measure the flux densities, we used the AIPS++ VIEWER program[3] to

---

[3]This capability is now available within CASA software.

create identical polygonal apertures around each of our sources at 3 and 6 cm for the ATCA data and at 1.3 and 3.6 cm for the VLA data. By using identical convolution kernels and apertures, we are able to maximize the accuracy of the relative photometry. Errors in the flux densities were determined by adding in quadrature the uncertainties due to the absolute flux calibration, variation from the sky background, and changes in the size and shape of the aperture. For the purposes of determining the uncertainties in the spectral index α, the final term in the uncertainty due to variation in aperture is neglected as identical apertures are used at both frequencies. See Tables 3 and 4 for integrated and peak flux densities as well as spectral indices of each source.

3.1. Ionizing Luminosities and Cluster Masses

Massive, short-lived stars drive the thermal free-free emission we observe at radio wavelengths; hence, an understanding of the photo-ionization rate for each of our candidate UDHII regions enables us to predict the number of massive stars in a cluster. Lyman continuum photons ionize these HII regions; thus, with knowledge of the radio luminosities, we can predict a lower bound on the Lyman continuum flux (Condon 1992),

$$Q_{\mathrm{Lyc}} \geq 6.3 \times 10^{52}\,\mathrm{s^{-1}} \left(\frac{T_e}{10^4\,\mathrm{K}}\right)^{-0.45} \left(\frac{\nu}{\mathrm{GHz}}\right)^{0.1} \left(\frac{L_{\mathrm{thermal}}}{10^{27}\,\mathrm{erg\,s^{-1}\,Hz^{-1}}}\right). \tag{2}$$

A number of possible issues must be kept in mind when interpreting the Q_{Lyc} values and radio flux densities. First, the application of this equation assumes the emission is purely thermal and optically thin. Contamination from non-thermal emission within the synthesized beams is also a possible issue at the spatial resolutions used here, and would inflate the resulting Q_{Lyc} values. To partially mitigate these issues, it is advantageous to use flux densities obtained at the highest radio frequency available for two reasons: (1) the higher frequency emission suffers from less self-absorption and is therefore more likely to be optically thin, and (2) the higher the frequency, the less likely it is to contain a significant amount of non-thermal contaminating flux. Second, an electron temperature must also be assumed, and we adopt a "typical" HII region temperature of $T_e = 10^4$ K; the uncertainty in Q_{Lyc} due to this assumption is $\lesssim 20\%$. Finally, the actual Q_{Lyc} values could be higher than observed if a significant fraction of the ionization radiation is either absorbed by dust within the HII region or suffers from significant leakage through a porous ISM. Thus, when these conditions are met, the Q_{Lyc} values quoted here should be interpreted as lower limits.

The inferred values for Q_{Lyc} of each of the identified thermal sources are shown in Table 5. Assuming each of these thermal sources contains an embedded star cluster, we also estimate the number of O7.5 V stars, each having a Lyman continuum flux $Q_{\mathrm{Lyc}} = 1.0 \times 10^{49}$ s^{-1} (Vacca 1994), required to produce the observed free-free, thermal radio flux (see Table 5).

We used the stellar synthesis code Starburst99 (Leitherer et al. 1999) in combination with Q_{Lyc} to estimate the total stellar masses of the natal clusters. Following Johnson et al. (2003), we

assume each cluster has a metallicity $Z = 0.04$ and a Salpeter IMF from 1 to 100 $M_\odot$. Assuming the Q_{Lyc} values scale directly with the cluster mass and that the clusters are $\lesssim 3$ Myr old, we infer stellar masses for the radio detected star-forming regions ranging between $\sim 10^4$ $M_\odot$ and 10^6 $M_\odot$ (see Table 5). The most massive of these star-forming regions also appear to be slightly spatially extended at the resolution of these observations and likely include a number of star clusters that are not resolved.

3.2.   Inferred Sizes of Thermal Sources

In order to determine the sizes of the detected sources in Table 5, we initially fit a Gaussian profile to each source, from which the synthesized beam was deconvolved in order to estimate the actual source sizes. The major limitation of this method is that it requires the source to be roughly Gaussian, which is not true for many sources presented here, some of which appear to have quite complex structure. Nevertheless, this method will, at a minimum, provide information about whether or not a source is extended at the resolution of the observation. Using this method, we infer the physical sizes of the star forming regions based upon the distances in Table 6 and deconvolved angular sizes in Tables 3 and 4, with resulting sizes ranging between ~ 20 pc to a few ~ 100 pc. These sizes are much larger than one would expect for an individual cluster (a few pc); thus we conclude that most of the radio-detected star-forming regions presented here are likely to be groups of individual clusters, which may well be at slighltly different evolutionary states. Furthermore, these large inferred sizes allow for a complex origin for the observed emission and potential non-thermal contamination; there is ample room within these large regions for a large number of ultracompact HII regions, evolved HII regions, SNR, and other objects. Higher spatial resolution observations are clearly required in order to disentangle the components of the complex sources and facilitate more precise size measurements.

3.3.   Comparison to Cas A and W49A

In order to provide a comparison for the relative fluxes of non-thermal and thermal sources, we calculate the expected flux densities and detection thresholds for the Galactic supernova remnant Cas A, an UCHII region complex W49A at the distance of the galaxies in this sample. Cas A is the canonical "young" core collapse SNR in the galaxy, with the highest luminosity and youngest age of any such remnant in the Milky Way (Baars et al. 1977; Fesen et al. 2006). Likewise, W49A is a benchmark star-forming region in the galaxy, with ~ 30 individual thermal radio sources and Q_{Lyc} 10^{51} s^{-1} (e.g. De Pree et al. 2000). The expected signal-to-noise for analogs to Cas A and W49A in our sample galaxies at 3.6 cm are shown in Table 6. For example, if Cas A would have been a $\sim 1\sigma$ detection in a given galaxy, we would be unlikely to identify an individual supernova remnant. If W49A would have been a detection $\gtrsim 5\sigma$ in a given galaxy and yet no thermal sources are detected, such a detection limit would suggest no current star formation above this limit in

that galaxy.

Given our detection limits for objects similar to Cas A and W49A, there are a few striking non-detections that merit further investigation. For example, in the galaxy Mrk 1479 ($\sim 4.9 - 5.1$ Mpc, Tully 1988; Marakova & Karachentsev 1998), Cas A and W49A would have exhibed detections at the level of $\sim 10\sigma$ and 6σ, respectively; yet no radio sources are detected. The lack of such natal clusters could suggest that the current star formation rate in Mrk 1479 is below that of the Milky Way. However, the inclusion of Mrk 1479 in both the Markarian catalog of ultraviolet bright galaxies and Vorontsov-Velyaminov (VV) catalog of interacting galaxies suggests that it must have recently been undergoing vigorous star formation. Thus, the lack of detected thermal radio sources in this case supports the hypothesis that the natal stage of a cluster's evolution is extremely short.

4. Conclusions

In this radio study of 25 galaxies selected based upon their optical signposts of star formation, we expected to detect a number of thermal radio sources originating from massive nascent star clusters. However, we only detect definite thermal-dominated radio sources in five of the sample galaxies, with an additional six galaxies hosting radio sources whose origins are ambiguous within uncertainties. Using the benchmark Galactic star-forming region W49A, we put these non-detections in context; in several galaxies, W49A would have been a $\gtrsim 3 - 5\sigma$ detection. For example, Mrk 1479 is a notable case of a UV galaxy, included in both the VV and Markarian catalogs, with no evidence of thermal radio emission coming from an object similar to W49A at a $\sim 6\sigma$ level. For the five galaxies with detected thermal radio sources, the inferred properties of the nascent clusters range from large OB-associations to moderate super star clusters—extending both above and below the mass of W49A.

One hypothesis to explain the dearth of natal clusters in this sample is that the timescale a star-forming region spends in a stage that is detectable in radio is extremely brief. Johnson (2004) suggest that SSCs may spend as little as ~ 0.5 to 1 Myr in the embedded phase when they are detectable with thermal radio emission. Compared to galaxy evolution timescales, the time interval for star formation is very short. Our results are consistent with this hypothesis, however a more complete statistical sample is needed to better constrain the timescales. Such a larger and complete sample would allow us to compare the number of clusters in different evolutionary stages and track the emergence process.

While this study was intended to identify candidate natal star-forming regions in nearby galaxies, follow-up efforts are imperative. In particular, this work would benefit from higher spatial resolution observations than those presented here. Such observations will be critical for disentangling thermal and non-thermal sources in close proximity. In addition, higher frequency radio observations will provide much stronger constraints on the the spectral energy distributions of the thermal radio sources. In particular, high spatial resolution observations at $\sim 20 - 50$ GHz will be

useful for better understanding the relationship between between cluster properties and the local environment in which they are formed.

Facilities: VLA, ATCA

A.   Notes on Individual Galaxies in this Sample

A.1.   Galaxies Observed with the VLA

Arp 217

Arp 217 (NGC 3310, VV 356/406, UGC 5786)—peculiar SAB(r)bc galaxy with giant HII regions that may have merged with another galaxy in the past (Sharp 1996). Situated at 19.6 Mpc with an angular size of $3'.1 \times 2'.4$, it contains W-R stars in its HII clouds, which are 12 arcsec southwest of its nucleus (Zezas et al. 1998). Rosa-González et al. (2007) estimate the SFR of Arp 217 to be 7.6 $M_\odot$ yr^{-1} and 9.8 $M_\odot$ yr^{-1} based on Hα and 1.4 GHz magnitudes, respectively. Using *ROSAT* and *ASCA* observations, Zezas et al. (1998) find hard x-ray emission in the direction of Arp 217. Based on observations at other wavelengths, this x-ray source could not be an AGN; therefore, Zezas et al. (2004), using *Chandra*, conclude that the source of x-rays is due to star formation. Elmegreen et al. (2002) find 17 superstar cluster candidates in the southern spiral arm of Arp 217.

Arp 233

Arp 233 (Haro 2, Mrk 33, or UGC 05720)—irregular, BCD galaxy of $1'.12 \times 0'.80$ at ∼22 Mpc. In their optical survey of BCD galaxies, Gil de Paz et al. (2003) deduce that because Arp 233 has a B-band absolute magnitude $M_B < -18.15$ and a K-band absolute magnitude $M_K > -21$, it must be experiencing a massive starburst. Summers et al. (2001) estimate, based on evolutionary synthesis models and M_B, that the age of the Arp 233 starburst is 5.8 Myr and that its mass is 6.9×10^6 $M_\odot$.

Mrk 35

Mrk 35 (NGC 3353, UGC 5860, Haro 3)—a BCD galaxy of $1'.20 \times 0'.83$. At ∼13.1 Mpc it has an optical diameter of 3.8 kpc (Steel et al. 1996). Since W-R stars have been found in Mrk 35,

it must have undergone recent star formation with a peak starburst event occurring within the last $\sim$3-6 Myr (Johnson et al. 2004).

NGC 4490

NGC 4490 (UGC 7651, Arp269, VV 30a)—peculiar SB(s)d galaxy at $\sim$8.4 Mpc which has interacted with NGC 4485, northwest of NGC 4490. Elmegreen et al. (1998) have determined, with N-body simulations and an analysis of tidal morphologies, that the two interacting galaxies collided 4×10^8 yr ago, about the same time the youngest star forming regions in the galaxy pair formed. Clemens et al. (1998) observed with the VLA a large H I envelope surrounding the galaxies and discuss the possibility that the H I might be primordial gas from which the NGC 4490/4485 pair formed.

Arp 32

Arp 32 (UGC 10770, VV89)—peculiar type SBm galaxy pair at a distance of $\sim$17 Mpc. Damjanov et al. (2006) performed multi-wavelength photometry on Arp 32 with GALEX UV, KPNO-4m optical, near-IR, *Spitzer* infrared, and 20 cm VLA radio data. They formed an SED of the galaxy pair and fit it to a galaxy model. The best fit model to the upper companion of Arp 32 suggests that it is an elliptical galaxy with a 5 Gyr stellar population with 10-30% of the stars < 1 Gyr. For the lower component of Arp 217, the UV SFR is 0.12 $M_\odot$ yr^{-1} while the IR SFR is larger, 1 $M_\odot$ yr^{-1}; this suggests obscured star formation.

Arp 263

Arp 263 (NGC 3239, UGC 5637, VV 95)—peculiar IB(s)m galaxy at $\sim$9.1 Mpc. Krienke & Hodge (1990) use Hα and neutral hydrogen observations to detect evidence of new star formation in Arp 263. In addition to evidence of young star formation, they find a warped disk and tidal tails suggesting Arp 263 has interacted tidally with a currently unseen companion.

Arp 266

Arp 266 (NGC 4861, UGC 8098, IC 3961, VV 797, IZW49)—an SB(s)m starburst galaxy at $\sim$12 Mpc. Mrk 59 and I Zw 49 are the HII regions within the galaxy. From 4650 Å to 4750 Å, García-Lorenzo et al. (1999) find a W-R emission bump in the spectra of the nuclear, $\sim 10'' \times 12''$ region of Arp 266. In their continuum map, they observe that Arp 266 has an elongated morphology, common in W-R and merging galaxies. Barth et al. (1994) observed—in Hα, Hβ, and [O III] λ5007—28 HII regions in Arp 266. They note a correlation between the equivalent widths of Hβ emission and the excitation index $\log([\text{O III}]/\text{H}\beta)$.

Arp 277

Arp 277 (VV 313)—a galaxy pair composed of two Im galaxies at $\sim$12 Mpc: NGC 4809 and NGC 4810. NGC 4809 is the brighter of the two strongly-interacting galaxies. Casasola et al. (2004) report that NGC 4809 has an optical diameter of 5.0 kpc, blue luminosity of $\log L_B = 8.18$ L$_\odot$, dust mass of 5.4×10^4 M$_\odot$, H I mass of 9.3×10^8 M$_\odot$, and a FIR luminosity of $\log L_{FIR} = 8.32$ L$_\odot$. The H I mass and FIR luminosity, however, may include emission from both NGC 4809 and NGC 4810. From optical spectroscopy of its ionized gas, NGC 4809 has an average $T_e \sim 11300$ K, an average electron density of 98 cm^{-3}, and an oxygen abundance of $12 + \log\ [O/H] = 8.21$ dex ($\sim$1/3 Z$_\odot$) (Kniazev et al. 2004). NGC 4810 has a blue magnitude of -16.1 mag (Albrecht et al. 2004). Using the Hα flux, James et al. (2004) measured the SFR of NGC 4809 as 0.25 M$_\odot$ yr^{-1} and NGC 4810 as 0.13 M$_\odot$ yr^{-1}.

Arp 291

Arp 291 (UGC 5832, VV 112)—is a peculiar, ring galaxy at $\sim$15 Mpc. It has an optical diameter of 5.5 kpc, blue luminosity of $\log L_B = 8.81$ L$_\odot$, dust mass of 8.1×10^4 M$_\odot$, H I mass of 5.5×10^8 M$_\odot$, and a FIR luminosity of $\log L_{\rm FIR} = 8.50$ L$_\odot$ (Casasola et al. 2004). Arp 291 has an NVSS 1.4 GHz flux of 4.1 mJy and $\log L_{1.4\rm GHz} = 20.39$ W Hz^{-1} (Condon et al. 2002). At this luminosity the radio emission is most likely related to star formation and not an AGN, which implies a star formation rate of 0.2 M$_\odot$ yr^{-1} (Condon 1992). Arp 291 is part of a group of galaxies behind the M 96 group and has M$_{\rm HI} \sim 3 \times 10^8$ M$_\odot$ and a dynamical mass of $\sim 2 \times 10^9$ M$_\odot$ (Schneider 1989).

Mrk 1063

Mrk 1063 (NGC 1140, VV 482)—Seyfert type 2, dwarf, peculiar IBm galaxy at $\sim$20 Mpc. Using *HST*'s Planetary Camera, Hunter et al. (1994) find 6–7 SSCs in the central 0.5 kpc of Mrk 1063. de Grijs et al. (2004) find, based on the [Fe II] 1.6 μm emission line observed with Gemini South, that both the star formation regions of Mrk 1063 have a supernova rate of $\gtrsim 0.3$ SN yr^{-1}. They find that the young massive cluster (YMC) ages are all $\lesssim 20$ Myr.

Mrk 1080

Mrk 1080 (NGC 1507, UGC 2947)—edge-on SB(s)m galaxy at $\sim$11 Mpc. While Mrk 1080 is optically isolated with no bright companions, it does have an H I-rich companion with $M_{\rm HI} = 2.6 \times 10^7$ M$_\odot$ and a dynamical mass of 2×10^9 M$_\odot$ (Wilcots et al. 1996). The H I distribution of Mrk 1080 also appears to be warped in the outer parts, possibly indicative of a recent interaction. It is an isolated galaxy with a blue luminosity of 2×10^9 L$_\odot$ and $L_{\rm FIR} = 5 \times 10^8$ L$_\odot$ (Lisenfeld et al. 2007), and is relatively gas-rich with $M_{\rm HI}/L_B = 0.33$ M$_\odot$ L$_\odot^{-1}$. Estimates of the star formation

rate range from 0.035 $M_\odot$ yr^{-1} (Meurer et al. 2006) from Hα observations and 0.15 $M_\odot$ yr^{-1} calculated from the FIR using (Kennicutt 1998) to 0.3 $M_\odot$ yr^{-1} from 1.4 GHz radio continuum (Condon et al. 2002). Miller & Veilleux (2003) have detected extra-planar diffuse Hα emission in this galaxy, indicating that the star formation in Mrk 1080 strongly influences its morphology.

Mrk 1346

Mrk 1346 (NGC 5107, UGC 8396)—type SB(s)d galaxy at ∼14 Mpc. van Moorsel (1983) detect with the Westerbork Synthesis Radio Telescope a mass of H I northwest of the optical bulge of Mrk 1346. Leroy et al. (2005) place an upper limit on the CO in this galaxy of $\lesssim$ 0.87 K km s^{-1}. James et al. (2004) report a SFR of 0.75$M_\odot$ yr^{-1}.

Mrk 1479

Mrk 1479 (NGC 5238, VV 828, SBS 1331+518, IZW64)—type SAB(s)dm galaxy at ∼5 Mpc. This galaxy is a BCD and part of both the Markarian and VV catalogs, indicating that it is both UV-bright, and also shows signs of interaction; Vorontsov-Velyaminov (1977) classify it as a interacting double system. Arkhipova et al. (1987) note intense Hα emission along the length of the galaxy, and estimate its diameter as ∼ 2 kpc. Huchtmeier & Richter (1988) estimate its total mass as ∼ 3×10^8 $M_\odot$.

Mrk 86

Mrk 86 (NGC 2537, UGC 4274, Arp 6, VV 138)—peculiar SB(s)m galaxy at ∼6 Mpc. Gil de Paz et al. (2000) have found three distinct stellar populations in Mrk 86, one of which is a 30 Myr old central starburst with a mass of ∼ 9×10^6 $M_\odot$. They also note that there must be a global triggering mechanism responsible for forming the at least 46 young star formation regions. Gil de Paz et al. (2002) observed the ^{12}CO $J = 1 - 0$ and $J = 2 - 1$ lines of Mrk 86 and found a horseshoe-shaped distribution of gas surrounding the galaxy's nuclear starburst.

Mrk 370

Mrk 370 (NGC 1036, UGC 2160, IC 1828)—a BCD, peculiar galaxy at ∼12 Mpc. Cairós et al. (2002) can reproduce their observed photometry of Mrk 370 if they assume an instantaneous starburst with a Salpeter initial mass function (IMF) with a mass limit of 100 $M_\odot$. They find that this starburst is ∼ $3 - 6$ Myr old.

Mrk 829

Mrk 829 (UGC 09560, IIZW70, VV 324b)—peculiar, BCD galaxy at ∼18 Mpc that is

interacting with IIZW71. Rosa-González et al. (2007) estimate the SFR of Mrk 829 based on Hα and 1.4 GHz to be 0.2 and 0.1 M$_\odot$ yr^{-1}, respectively. Kehrig et al. (2008) detect HeII λ4686 emission, indicating hard ionizing radiation related to young massive stars. Kehrig et al. also determine an oxygen abundance for this system of $12 + \log(\mathrm{O/H}) = 7.65 - 8.05$.

<div align="center">NGC 1156</div>

NGC 1156 (UGC 2455, VV 531)—galaxy of type IB(s)m at $\sim$6 Mpc. Karachentsev et al. (1996), after finding a distance to this Magellanic-type galaxy, note that it is "one of the least disturbed galaxies in the Nearby Universe" and that it is isolated from other galaxies. Despite its seeming quiescence, NGC 1156 shows signatures of recent star formation activity: W-R emission features and HII emission (Ho et al. 1995). Vacca & Conti (1992) argue that the number ratios of W-R- to O-type stars in galaxies showing W-R features indicate that the galaxy's star formation must be occurring in short bursts of timescales $\leq 10^6$ yr.

<div align="center">NGC 3003</div>

NGC 3003 (UGC 5251)—type SBbc, W-R galaxy. Although there is a W-R bump detected in NGC 3003 (Ho et al. 1995), there is also a notable lack of broad Hα component compared to other galaxies (Schaerer et al. 1999). Rossa & Dettmar (2003) note that the ratio of 60μm to 100μm fluxes suggests enhanced dust temperatures due to star formation activity. Rossa & Dettmar also find strong planar Hα emission along with several bright Hα emission knots.

A.2. Galaxies Observed with the ATCA

<div align="center">NGC 1313</div>

NGC 1313 (VV 436)—With the largest angular extent of any of the southern hemisphere galaxies in this sample, it spans $9'\!.1 \times 6'\!.9$. It is a face-on SB(s)d galaxy at $\sim$4.2 Mpc. NGC 1313 contains the radio-bright remnant of the Type II supernova SNR 1978K (Ryder et al. 1993). Larsen (2004) identifies many young stellar clusters with ground-based and *HST* WFPC2 data in NGC 1313. Based on an extensive H$\,$I (1.4 GHz) map by Peters et al. (1994), the kinematics of NGC 1313 suggest that it interacted with a dwarf galaxy that has pulled a loop of hydrogen gas out of its plane. Far infrared (FIR) magnitudes imply NGC 1313 has an area-normalized star formation rate (SFR) $\Sigma_{\mathrm{SFR}} = 4.04 \times 10^3$ M$_\odot$ yr^{-1} kpc^{-2} (Larsen & Richtler 2000), or an estimated 1.18×10^6 M$_\odot$ yr^{-1} throughout the whole galaxy. Wolf-Rayet (W-R) features are found at large galactocentric radii in NGC 1313 (Schaerer et al. 1999).

NGC 1510

NGC 1510—$1.'3 \times 0.'7$ type E0 galaxy with two central "condensations," one of which contains W-R stars (Schaerer et al. 1999; Conti 1991). Eichendorf & Nieto (1984) suggest that an interaction with the nearby NGC 1512 has triggered a starburst in NGC 1510. Storchi-Bergmann et al. (1994) estimate the current SFR of NGC 1510 to be 0.3 $M_\odot$ yr^{-1}.

NGC 1522

NGC 1522—$1.'2 \times 0.'8$ S0 peculiar galaxy at 10.6 Mpc. It has a $M_B = -16.1$ mag and a $\log L_{H\alpha} = 39.91$ ergs s^{-1} (Gil de Paz et al. 2003). The source has been detected by FUSE in the UV (Fox et al. 2006). Both the Hα flux and the UV brightness point towards prolific star formation occurring in NGC 1522. Loose & Thuan (1986) classify the galaxy as an iE BCD, meaning that it has elliptical outer isophotes and irregular inner isophotes due to star formation. Malin & Carter (1983) note that the outer envelope is displaced, so this galaxy shows signatures of its interaction with NGC 1510. It is located in the NGC 1566 group of galaxies and has an H I mass of 5×10^8 $M_\odot$ with a M_{HI}/L_B of 0.5 in solar units (Kilborn et al. 2005).

NGC 3125

NGC 3125 (Tol 3)—an irregular BCD galaxy with an angular size of $1.'1 \times 0.'7$. At a distance of 11.5 Mpc, it is comprised of two bright lobes (Schaerer et al. 1999). Hadfield & Crowther (2006) surveyed the W-R stars of this galaxy and found that there are fewer than suggested by previous UV studies. Alton et al. (1994) find, with an optical polarization map, that part of NGC 3125 is a reflection nebula illuminated by a central starburst region.

NGC 5408

NGC 5408 (Tol 116)—$1.'6 \times 0.'8$ IB(s)m dwarf starburst galaxy at 4.8 Mpc. Using ATCA and *Chandra* observations, Soria et al. (2006) detect an ultra-luminous X-ray source in NGC 5408 that may have formed in recent starburst activity. NGC 5408, however, is not known to contain W-R features (Schaerer et al. 1999).

NGC 2101

NGC 2101—a type IB(s)m pec galaxy at 13.3 Mpc[4]. Hunter & Elmegreen (2004) infer a total star formation rate of $\sim 0.2 M_\odot$ yr^{-1} or $\sim 0.06 M_\odot$ yr^{-1}kpc^{-2}, among the highest SFRs for any

---

[4]From the NASA Extragalactic Database (NED) http://nedwww.ipac.caltech.edu/

of the Im-type galaxies in their sample, and typical of the SFRs for blue compact dwarfs in their sample.

TOL 0957-278

TOL 0957-278 (TOL 2)—distance of 7.1 Mpc, $M_B = -15.19$ mag, and $\log L_{H\alpha} = 39.86$ ergs s^{-1} (Gil de Paz et al. 2003). Rosa-González et al. (2007) cites a slightly higher value for $\log L_{H\alpha} = 40.41$ and derived a star formation rate of 0.3 M$_\odot$ yr^{-1}. Loose & Thuan (1986) classify it as an iE BCD. It is a possibly merging HII galaxy with strong emission lines (Smith et al. 1976) and a possible signature of W-R stars (Kunth & Joubert 1985; Conti 1991; Vacca & Conti 1992; Méndez & Esteban 2000). The entire galaxy contains about 10^5 M$_\odot$ of ionizing stars—about 540 O5V equivalent stars. The largest optical knot has a linear size of 225 pc (Méndez & Esteban 2000). Ages of the knots, derived from optical emission lines and broadband colors, are $\sim$5-10 Myr (Méndez & Esteban 2000). The galaxy has an H I mass of 3×10^8 M$_\odot$ (Barnes & de Blok 2001).

REFERENCES

Albrecht, M., Chini, R., Krügel, E., Müller, S. A. H., & Lemke, R. 2004, A&A, 414, 141

Alton, P. B., Draper, P. W., Gledhill, T. M., Stockdale, D. P., Scarrott, S. M., & Wolstencroft, R. D. 1994, MNRAS, 270, 238

Arkhipova V.P., Noskova R.I., Sil'chenko O.K., Zasov A.V. 1987, PisAZ, 13, 575

Baars, J. W. M., Genzel, R., Pauliny-Toth, I. I. K., & Witzel, A. 1977, A&A, 61, 99

Barnes, D. G., & de Blok, W. J. G. 2001, AJ, 122, 825

Barth, C. S., Cepa, J., Vilchez, J. M., & Dottori, H. A. 1994, AJ, 108, 2069

Beck, S. C., Turner, J. L., & Kovo, O. 2000, AJ, 120, 244

Beck, S.C., Turner, J.L., & Gorjian, V. 2001, AJ, 122, 1365

Cairós, L. M., Caon, N., García-Lorenzo, B., Vílchez, J. M., & Muñoz-Tuñón, C. 2002, ApJ, 577, 164

Casasola, V., Bettoni, D., & Galletta, G. 2004, A&A, 422, 941

Clemens, M. S., Alexander, P., & Green, D. A. 1998, MNRAS, 297, 1015

Condon, J. J., Cotton, W. D., & Broderick, J. J. 2002, AJ, 124, 675

Condon, J. J. 1992, ARA&A, 30, 575

Conti, P. S. 1991, ApJ, 377, 115

Damjanov, I., Fadda, D., Marleau, F., Appleton, P., Choi, P., Lacy, M., Storrie-Lombardi, L., & Yan, L. 2006, ArXiv Astrophysics e-prints, arXiv:astro-ph/0604276

De Pree, C. G., Wilner, D. J., Goss, W. M., Welch, W. J., & McGrath, E. 2000, ApJ, 540, 308

Eichendorf, W., & Nieto, J.-L. 1984, A&A, 132, 342

Elmegreen, B. G., & Efremov, Y. N. 1997, ApJ, 480, 235

Elmegreen, D. M., Chromey, F. R., Knowles, B. D., & Wittenmyer, R. A. 1998, AJ, 115, 1433

Elmegreen, D. M., Chromey, F. R., McGrath, E. J., & Ostenson, J. M. 2002, AJ, 123, 1381

Fesen, R.A. et al. 2006, ApJ, 645, 283

Fox, A. J., Savage, B. D., & Wakker, B. P. 2006, ApJS, 165, 229

García-Lorenzo, B., Mediavilla, E., & Arribas, S. 1999, Wolf-Rayet Phenomena in Massive Stars and Starburst Galaxies, 193, 598

Gil de Paz, A., Zamorano, J., & Gallego, J. 2000, A&A, 361, 465

Gil de Paz, A., Silich, S. A., Madore, B. F., Sánchez Contreras, C., Zamorano, J., & Gallego, J. 2002, ApJ, 573, L101

Gil de Paz, A., Madore, B. F., & Pevunova, O. 2003, ApJS, 147, 29

Gorjian, V., Turner, J.L., & Beck, S.C. 2001, ApJ, 554, 29

Green, D. A. 1984, MNRAS, 209, 449

de Grijs, R., et al. 2004, MNRAS, 352, 263

Hadfield, L. J., & Crowther, P. A. 2006, MNRAS, 368, 1822

Ho, L. C., Filippenko, A. V., & Sargent, W. L. 1995, ApJS, 98, 477

Huchtmeier, W.K. & Richter, O.-G. A&A, 203, 237

Hunter, D. A., O'Connell, R. W., & Gallagher, J. S., III 1994, AJ, 108, 84

Hunter, D. A. & Elmegreen, B. G., 2004, AJ, 128, 2170

James, P. A., et al. 2004, A&A, 414, 23

Johnson, K. E. & Kobulnicky, H. A. 2003, ApJ, 597, 923

Johnson, K. E., Indebetouw, R., & Pisano, D. J. 2003, AJ, 126, 101

Johnson, K. E., Indebetouw, R., Watson, C., & Kobulnicky, H. A. 2004, AJ, 128, 610

Johnson, K. E., Hunt, L. K., & Reines, A. E. 2009, AJ, 137, 3788

Johnson, K. E. 2004, The Formation and Evolution of Massive Young Star Clusters, 322, 339

Karachentsev, I., Musella, I., & Grimaldi, A. 1996, A&A, 310, 722

Kennicutt, R. C., Jr., et al. 2003, PASP, 115, 928

Kennicutt, R. C., Jr. 1998, ARA&A, 36, 189

Kehrig, C., Vilchez, J. M., Sanchez, S. F., Telles, E., Perez-Montero, E., Martin-Gordon, D. 2008, A&A, 477, 813

Kilborn, V. A., Koribalski, B. S., Forbes, D. A., Barnes, D. G., & Musgrave, R. C. 2005, MNRAS, 356, 77

Kniazev, A. Y., Pustilnik, S. A., Grebel, E. K., Lee, H., & Pramskij, A. G. 2004, ApJS, 153, 429

Kobulnicky, H. A., & Johnson, K. E. 1999, ApJ, 527, 154

Krienke, K., & Hodge, P. 1990, PASP, 102, 41

Kunth, D., & Joubert, M. 1985, A&A, 142, 411

Lada, C. J. & Lada, E. A., 2003 ARA&A, 41, 57]

Larsen, S. S., & Richtler, T. 2000, A&A, 354, 836

Larsen, S. S. 2004, A&A, 416, 537

Leitherer, C., et al. 1999, ApJS, 123, 3

Leroy, A., Bolatto, A. D., Simon, J. D., & Blitz, L. 2005, ApJ, 625, 763

Lisenfeld, U., et al. 2007, A&A, 462, 507

Loose, H.-H., & Thuan, T. X. 1986, in Star Forming Dwarf Galaxies and Related Objects, ed. D. Kunth, T. X. Thuan, & J. T. T. Van (Gif-sur-Yvette: Editions Frontiéres), 73

Malin, D. F., & Carter, D. 1983, ApJ, 274, 534

Makarova, L. N. & Karachentsev, I. D. 1998, A&AS

Meurer, G. R., et al. 2006, ApJS, 165, 307

Mezger, P. G., & Henderson, A. P. 1967, ApJ, 147, 471

Méndez, D. I., & Esteban, C. 2000, A&A, 359, 493

Miller, S. T., & Veilleux, S. 2003, ApJS, 148, 383

Peters, W. L., Freeman, K. C., Forster, J. R., Manchester, R. N., & Ables, J. G. 1994, MNRAS, 269, 1025

Reines, A. E., Johnson, K. E., & Goss, W. M. 2008, AJ, 135, 2222

Rosa-González, D., Schmitt, H. R., Terlevich, E., & Terlevich, R. 2007, ApJ, 654, 226

Rossa, J. & Dettmar, R. J. 2003, A&A, 406, 505

Ryder, S., Staveley-Smith, L., Dopita, M., Petre, R., Colbert, E., Malin, D., & Schlegel, E. 1993, ApJ, 416, 167

Schaerer, D., Contini, T., & Pindao, M. 1999, A&AS, 136, 35

Schneider, S. E. 1989, ApJ, 343, 94

Sharp, N. A. 1996, Bulletin of the American Astronomical Society, 28, 1359

Smith, M. G., Aguirre, C., & Zemelman, M. 1976, ApJS, 32, 217

Soria, R., Fender, R. P., Hannikainen, D. C., Read, A. M., & Stevens, I. R. 2006, MNRAS, 368, 1527

Steel, S. J., Smith, N., Metcalfe, L., Rabbette, M., & McBreen, B. 1996, A&A, 311, 721

Storchi-Bergmann, T., Calzetti, D., & Kinney, A. L. 1994, ApJ, 429, 572

Summers, L. K., Stevens, I. R., & Strickland, D. K. 2001, MNRAS, 327, 385

Tarchi, A., Neininger, N., Greve, A., Klein, U., Garrington, S. T., Muxlow, T. W. B., Pedlar, A., & Glendenning, B. E. 2000, A&A, 358, 95

Tully, R. B. 1988, "Nearby Galaxies Catalog", Cambridge and New York, Cambridge University Press

Turner, J. L., Ho, P.T.P, & Beck, S. C. 1998, AJ, 116, 1212

Vacca, W. D., & Conti, P. S. 1992, ApJ, 401, 543

Vacca, W. D. 1994, ApJ, 421, 140

Vacca, W.D., Johnson, K.E. & Conti, P.S. 2002, AJ, 123, 772

Vorontsov-Velyaminov, B. A. 1977, A&AS, 28, 1

Weiler, K. W., Sramek, R. A., Panagia, N., van der Hulst, J. M., Salvati, M. 1986, ApJ, 301, 790

Whitmore, B.C. 2002, in: A Decade of Hubble Space Telescope Science, M. Livio, K. Noll, M. Stiavelli, Eds. (Cambridge Univ. Press, Cambridge, 2002), pp. 153-180.

Wilcots, E. M., Lehman, C., & Miller, B. 1996, AJ, 111, 1575

de Wit, W. J., Testi, L., Palla, F., Zinnecker, H. 2005, A&A, 437, 247

van Moorsel, G. A. 1983, A&AS, 53, 271

Wood, D. O. S., & Churchwell, E. 1989, ApJS, 69, 831

Zezas, A. L., Georgantopoulos, I., & Ward, M. J. 1998, MNRAS, 301, 915

Zezas, A., Georgantopoulos, I., Ward, M., Fabbiano, G., & Prestwich, A. 2004, Bulletin of the American Astronomical Society, 36, 964

Table 1.   Observed Galaxies with the VLA and the ATCA

Galaxy	Alternate Name	Classification(s)[a]	Distance (Mpc)
VLA Targets			
Arp 217	NGC 3310	SAB(r)bc pec HII	14.4
Arp 233	Haro 2	Im pec HII	20.4
Arp 263	NGC 3239	IB(s)m pec	9.1
Arp 266	NGC 4861	SB(s)m: Sbrst	11.9
Arp 277	VV313	Mult pec	11.8
Arp 291	UGC 05832	Mult pec	15.4
Arp 32	UGC 10770	SBm pec	17.8
Mrk 1063	NGC 1140	IBm pec:;HII Sy2	20.2
Mrk 1080	NGC 1507	SB(s)m pec?	11.1
Mrk 1346	NGC 5107	SB(s)d? sp	13.8
Mrk 1479	NGC 5238	SAB(s)dm	4.9
Mrk 35	NGC 3353	BCD/Irr HII	13.8
Mrk 370	NGC 1036	Pec?	11.7
Mrk 829	UGC 09560	pec; BCDG HII	17.5
Mrk 86	NGC 2537	SB(s)m pec	6.14
NGC 1156	UGC 02455	IB(s)m	6.11
NGC 3003	UGC 05251	SBbc	19.8
NGC 4490	ARP 269	SB(s)d pec	8.36
ATCA Targets			
NGC 1313	ESO 082- G 011	SB(s)d HII	4.19
NGC 1510	ESO 250- G 003	SA0 0 pec?;HIIBCDG	10.4
NGC 1522	ESO 156- G 038	(R')S0 0 : pec	10.0
NGC 2101	ESO 205- G 001	IB(s)m pec	13.7
NGC 3125	ESO 435- G 041	S BCDG	12.3
NGC 5408	ESO 325- G?047	IB(s)m HII	5.01
TOL 0957-278	ESO 435-IG 020	Merger? HII	10.4

[a]From the NASA Extragalactic Database (NED) http://nedwww.ipac.caltech.edu/

Table 2.   Imaging Parameters of the Observed Galaxies

Galaxy	Band (cm)	Convolved Beam Size[a] (arcsec)	Position Angle (deg)	Noise (μJy bm^{-1})
VLA Targets				
Arp 217	3.6	1.0×0.8	-81.7	26
	1.3	1.0×0.8	-81.7	39
Arp 233	3.6	1.0×0.8	-78.2	24
	1.3	1.0×0.8	-78.2	37
Arp 263[b]	3.6	0.4×0.3	-57.8	24
Arp 266[b]	3.6	0.3×0.2	79.9	27
Arp 277[b]	3.6	0.3×0.3	40.2	26
Arp 291[b]	3.6	0.3×0.3	-50.4	26
Arp 32[b]	3.6	0.3×0.3	-44.8	24
GO 20127[b]	3.6	0.2×0.2	-7.0	36
Mrk 1063[b]	3.6	0.4×0.2	-22.1	22
Mrk 1080[b]	3.6	0.4×0.2	-31.1	24
Mrk 1346[b]	3.6	0.3×0.2	86.3	25
Mrk 1479[b]	3.6	0.3×0.2	-85.0	24
Mrk 35	3.6	0.9×0.8	-85.2	25
	1.3	0.9×0.8	-85.2	49
Mrk 370[b]	3.6	0.3×0.2	-33.2	22
Mrk 829[b]	3.6	0.3×0.2	-83.7	24
Mrk 86[b]	3.6	0.3×0.2	-82.4	27
NGC 1156[c]	3.6	0.3×0.2	-49.4	26
NGC 3003[b]	3.6	0.5×0.3	-63.7	30
NGC 4490	3.6	0.8×0.7	12.6	55
	1.3	0.8×0.7	12.6	20
ATCA Targets				
NGC 1313	3	2.2×1.5	-5.8	48
	6	2.2×1.5	-5.8	53
NGC 1510	3	2.6×1.7	1.0	41
	6	2.6×1.7	1.0	48
NGC 1522	3	2.3×1.7	-3.5	44
	6	2.3×1.7	-3.5	45
NGC 2101	3	2.9×2.0	-5.7	36
	6	2.9×2.0	-5.7	42
NGC 3125	3	3.6×1.7	0.4	57
	6	3.6×1.7	0.4	61
NGC 5408	3	2.6×1.7	0.1	60
	6	2.6×1.7	0.1	48
TOL 0957-278	3	5.4×1.8	-6.3	68
	6	5.4×1.8	-6.3	78

[a]Applied via convolution in the imaging process

[b]No radio sources detected in 3.6 cm observations, and thus 1.3 cm observations were not pursued.

[c]Only one band available

Table 3.　Observed Properties of Detected VLA Radio Sources

Source	α (J2000)	δ (J2000)	Deconvolved Size[b] (arcsec)	Physical Size (pc)	$F_{1.3cm}$ (mJy)	Peak $F_{1.3cm}$ (mJy bm^{-1})	$F_{3.6cm}$ (mJy)	Peak $F_{3.6cm}$ (mJy bm^{-1})	α[c]
Arp 233n[a]	10 32 31.80	+54 24 04.0	1.8×1.2	180×120	1.1 ± 0.2	0.3 ± 0.1	0.8 ± 0.2	0.3 ± 0.1	0.3 ± 0.2
Arp 233s	10 32 31.97	+54 24 02.4	1.9×1.1	190×110	1.7 ± 0.4	0.6 ± 0.1	1.5 ± 0.5	0.7 ± 0.1	0.1 ± 0.3
Arp 217e[a]	10 38 44.83	+53 30 05.0	2.5×1.3	180×90	1.4 ± 0.3	0.6 ± 0.1	1.0 ± 0.2	0.5 ± 0.1	0.4 ± 0.2
Arp 217d	10 38 45.87	+53 30 12.1	0.5×0.5	40×40	1.3 ± 1.3	1.0 ± 0.1	1.7 ± 1.7	1.5 ± 0.1	—
Arp 217c	10 38 46.53	+53 30 06.4	0.2×0.2	10×10	0.2 ± 0.1	0.3 ± 0.1	0.4 ± 0.2	0.6 ± 0.1	-0.7 ± 0.4
Arp 217b	10 38 46.69	+53 30 11.8	1.7×1.1	120×80	0.5 ± 0.1	0.4 ± 0.1	0.5 ± 0.1	0.5 ± 0.1	-0.0 ± 0.2
Arp 217a	10 38 46.93	+53 30 16.8	0.9×0.7	60×50	0.6 ± 0.2	0.5 ± 0.1	0.5 ± 0.2	0.5 ± 0.1	0.2 ± 0.3
Mrk 35w[a]	10 45 21.96	+55 57 39.8	1.4×0.9	90×60	1.5 ± 0.2	0.8 ± 0.1	1.5 ± 0.3	0.9 ± 0.1	0.0 ± 0.2
Mrk 35e[a]	10 45 22.02	+55 57 40.1	1.2×1.0	80×70	1.3 ± 0.2	0.8 ± 0.1	1.2 ± 0.3	0.9 ± 0.3	0.1 ± 0.2
NGC 4490e	12 30 29.50	+41 39 28.4	0.5×0.4	20×20	1.0 ± 0.3	0.4 ± 0.1	1.0 ± 0.2	0.6 ± 0.1	0.0 ± 0.2
NGC 4490bw	12 30 34.44	+41 38 25.4	0.8×0.4	30×20	1.1 ± 0.3	0.4 ± 0.1	1.3 ± 0.4	0.7 ± 0.1	-0.2 ± 0.3
NGC 4490be[a]	12 30 34.50	+41 38 26.2	1.7×1.0	70×40	2.2 ± 0.5	0.5 ± 0.1	2.9 ± 0.6	0.8 ± 0.1	-0.3 ± 0.3
NGC 4490c	12 30 34.53	+41 38 33.3	0.5×0.5	20×20	0.5 ± 0.1	0.2 ± 0.1	0.9 ± 0.1	0.5 ± 0.1	-0.6 ± 0.1
NGC 4490d	12 30 34.91	+41 39 02.5	1.0×0.6	40×20	0.7 ± 0.1	0.2 ± 0.1	1.3 ± 0.2	0.4 ± 0.1	-0.7 ± 0.1
NGC 4490a	12 30 37.73	+41 37 58.8	0.8×0.6	30×20	1.1 ± 0.2	0.3 ± 0.1	0.8 ± 0.2	0.3 ± 0.1	0.2 ± 0.2

Note. — $\alpha = \log_{10}\left(F_{1.3cm}/F_{3.6cm}\right)/\log_{10}\left(\nu_{1.3cm}/\nu_{3.6cm}\right)$

Note. — See Table 2 for upper limits on non-detections' flux densities.

[a]Gaussian profile did not fit source.

[b]Sizes determined by best-fit Gaussian profile using the AIPS++ task IMAGEFITTER

[c]Uncertainty in α includes uncertainty due to flux calibration and background variation, but not uncertainty due to aperture size, which is identical at the two frequencies.

Table 4.   Observed Properties of Detected ATCA Radio Sources

Source	α (J2000)	δ (J2000)	Deconvolved Size[d] (arcsec)	Physical Size (pc)	F_{3cm} (mJy)	Peak F_{3cm} (mJy bm^{-1})	F_{6cm} (mJy)	Peak F_{6cm} (mJy bm^{-1})	α[e]
NGC 1313snr[b]	03 17 38.66	-66 33 03.6	0.4×0.5	10×10	21 ± 12	18 ± 1	27 ± 16	26 ± 1	-0.4 ± 0.6
NGC 1313b[a]	03 18 05.52	-66 30 25.2	1.4×1.3	30×30	1.1 ± 0.3	0.7 ± 0.1	1.1 ± 0.4	0.8 ± 0.1	0.0 ± 0.4
NGC 1313cw[c]	03 18 37.73	-66 29 33.7	1.5×1.6	30×30	0.1 ± 0.1	0.2 ± 0.1	0.3 ± 0.1	0.4 ± 0.1	-1.6 ± 0.5
NGC 1313ce[c]	03 18 38.05	-66 29 31.8	3.6×2.2	70×50	0.3 ± 0.1	0.2 ± 0.1	1.0 ± 0.2	0.5 ± 0.1	-2.0 ± 0.3
NGC 1313aw	03 18 45.15	-66 30 15.0	0.9×0.6	20×10	0.5 ± 0.2	0.5 ± 0.1	0.6 ± 0.2	0.6 ± 0.1	-0.2 ± 0.5
NGC 1313ae	03 18 46.04	-66 30 15.2	2.2×2.4	50×50	1.8 ± 0.3	0.5 ± 0.1	2.2 ± 0.3	0.9 ± 0.1	-0.3 ± 0.2
NGC 1510	04 03 32.80	-43 23 58.1	1.7×1.1	80×50	0.9 ± 0.6	0.7 ± 0.1	1.0 ± 0.6	0.7 ± 0.1	-0.1 ± 0.8
NGC 1522	04 06 08.13	-52 40 03.4	7.9×2.8	380×140	0.2 ± 0.1	0.1 ± 0.1	0.2 ± 0.1	0.3 ± 0.1	-0.0 ± 0.6
NGC 3125w	10 06 33.34	-29 56 06.8	2.2×1.7	130×100	3.1 ± 1.0	2.4 ± 0.1	3.2 ± 1.2	2.5 ± 0.1	-0.1 ± 0.4
NGC 3125e	10 06 33.98	-29 56 11.9	5.5×2.9	330×170	1.7 ± 0.7	0.9 ± 0.1	1.4 ± 1.0	1.0 ± 0.1	0.3 ± 0.6
NGC 5408s	14 03 18.35	-41 22 52.6	6.8×2.5	170×60	3.6 ± 0.8	1.4 ± 0.1	3.8 ± 0.9	1.5 ± 0.1	-0.1 ± 0.3
NGC 5408n	14 03 18.67	-41 22 50.0	4.5×2.1	110×50	0.3 ± 0.1	0.4 ± 0.1	0.3 ± 0.1	0.4 ± 0.1	-0.0 ± 0.3

Note. — $\alpha = \log_{10}\left(F_{3cm}/F_{6cm}\right)/\log_{10}\left(\nu_{3cm}/\nu_{6cm}\right)$

Note. — See Table 2 for upper limits on non-detections' flux densities.

[a]Larsen (2004) identifies this source as the star cluster n1313-341.

[b]Known supernova remnant 1978K.

[c]Gaussian profile did not fit source.

[d]Sizes determined by best-fit Gaussian profile using the AIPS++ task IMAGEFITTER.

[e]Uncertainty in α includes uncertainty due to flux calibration and background variation, but not uncertainty due to aperture size, which is identical at the two frequencies.
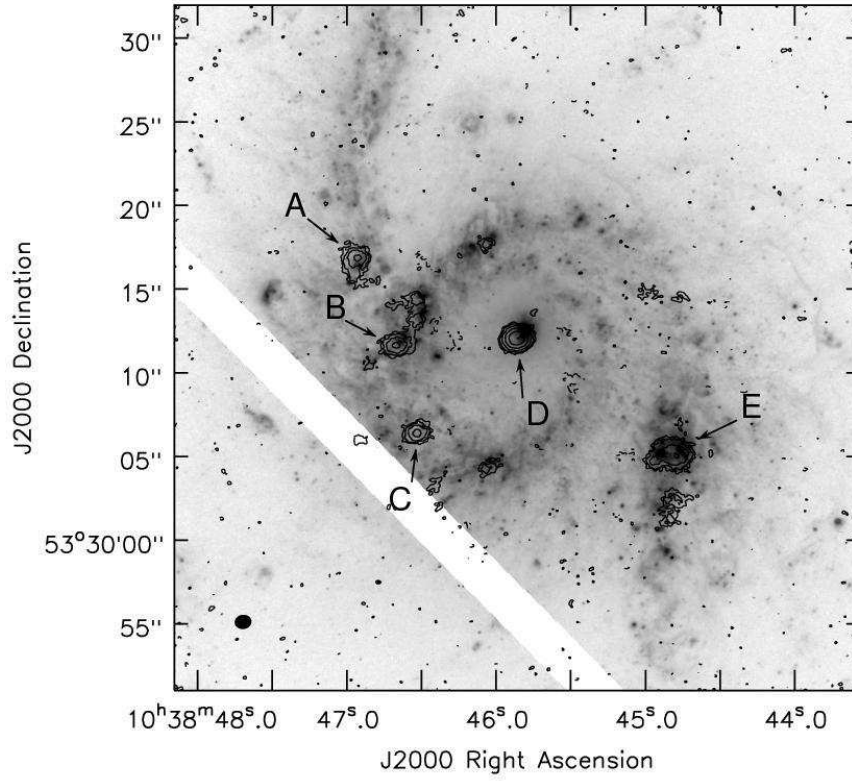
Fig. 1.— **Arp 217**. VLA 3.6 cm (8.5 GHz) radio contours of $-3, 3, 5, 9, 17, 33, 57 \times \sigma$ (26 μJy bm^{-1}) are overlaid on an *HST* F658N optical image. The beam size (1.0×0.8 arcsec) is indicated at the lower left. *HST* astronomy is precise to within ~ 1 arcsec.
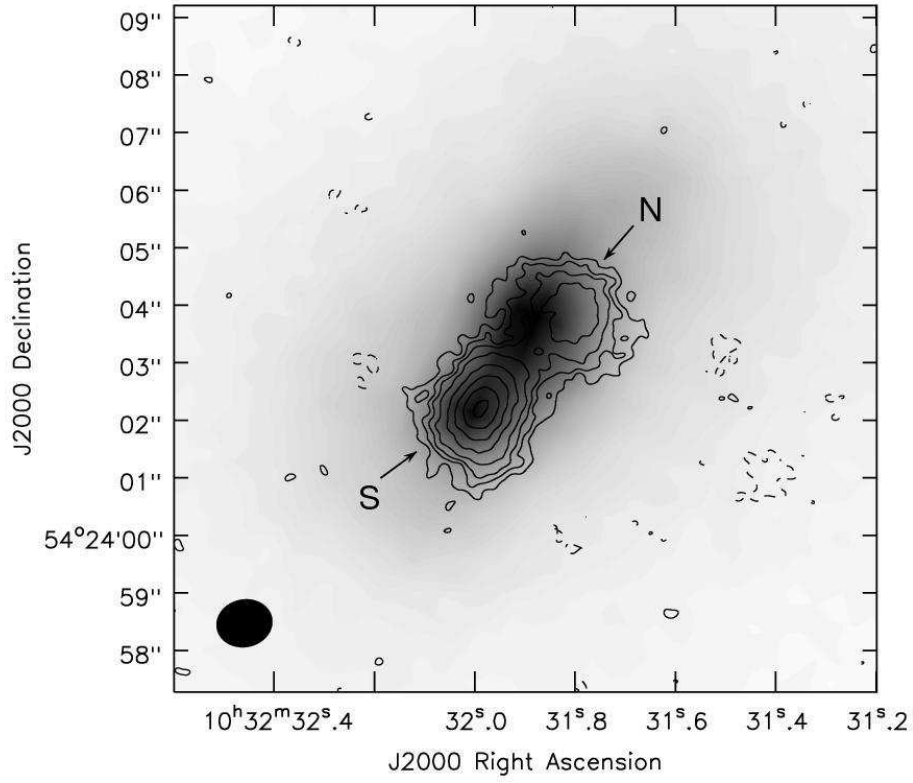
Fig. 2.— **Arp 233**. VLA 3.6 cm (8.5 GHz) radio contours of $-3, 3, 5, 7, 10, 15, 20, 25, 29 \times \sigma$ (24 μJy bm^{-1}) are overlaid on this Sloan Digitized Sky Survey (SDSS) z-band optical image. The beam size (1.0×0.8 arcsec) is indicated at the lower left.
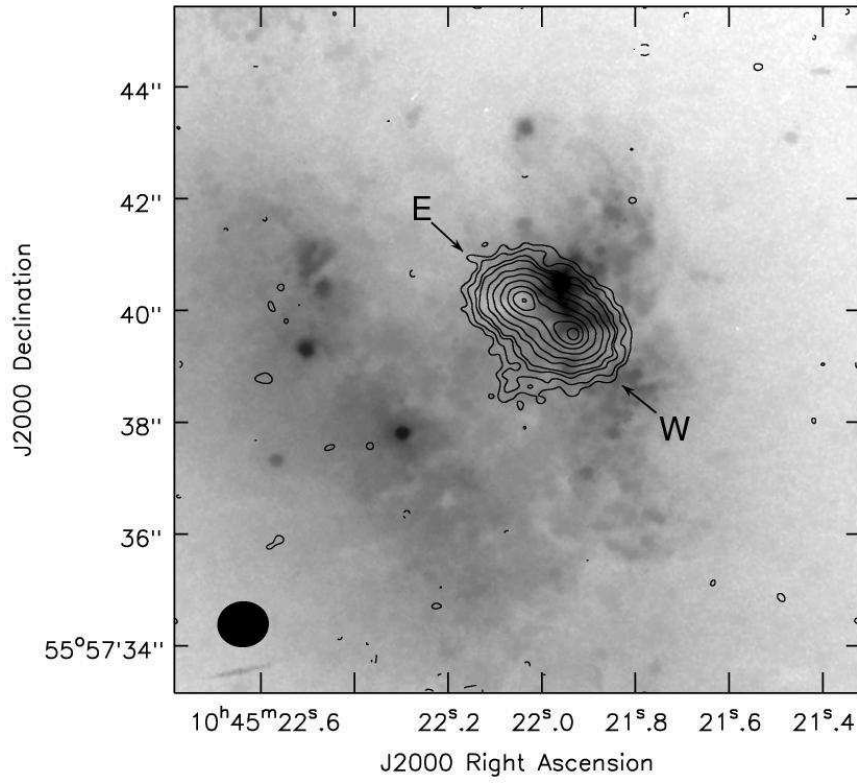
Fig. 3.— **Mrk 35**. VLA 3.6 cm (8.5 GHz) radio contours of $-3, 3, 5, 8, 10, 15, 20, 26, 31, 34, 36 \times \sigma$ $(25\ \mu\mathrm{Jy\ bm}^{-1})$ are overlaid on this *HST* F606W optical image. The beam size (0.9×0.8 arcsec) is indicated at the lower left. *HST* astronomy is precise to within ~ 1 arcsec.
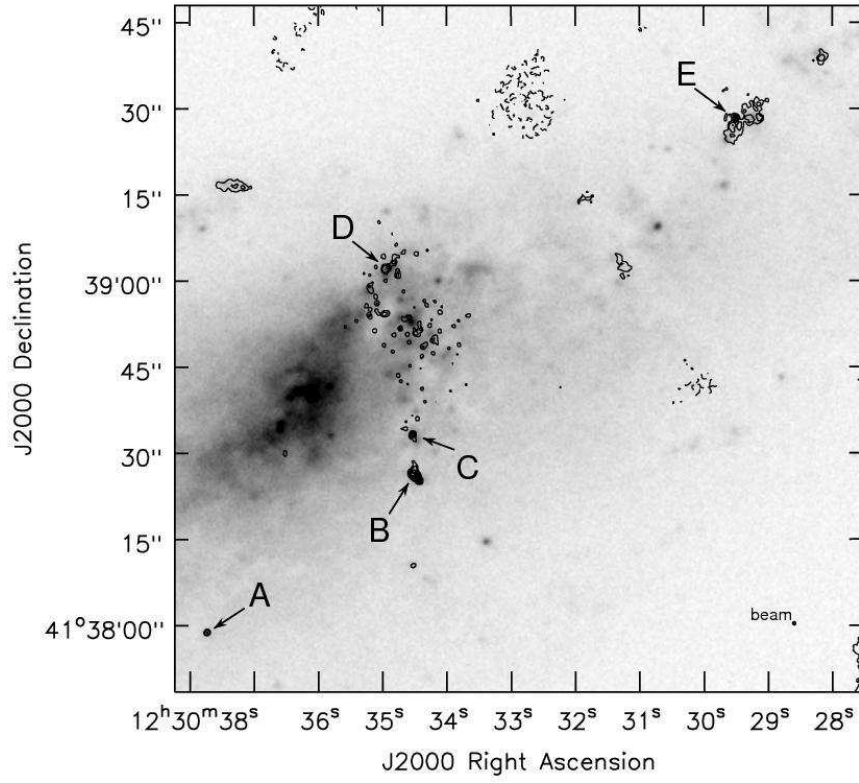
Fig. 4.— **NGC 4490**. VLA 3.6 cm (8.5 GHz) radio contours of $-3, 3, 4, 6, 8, 10, 12, 14 \times \sigma$ (55 μJy bm^{-1}) are overlaid on this SDSS z-band optical image. The beam size (0.8×0.7 arcsec is indicated at the lower left.
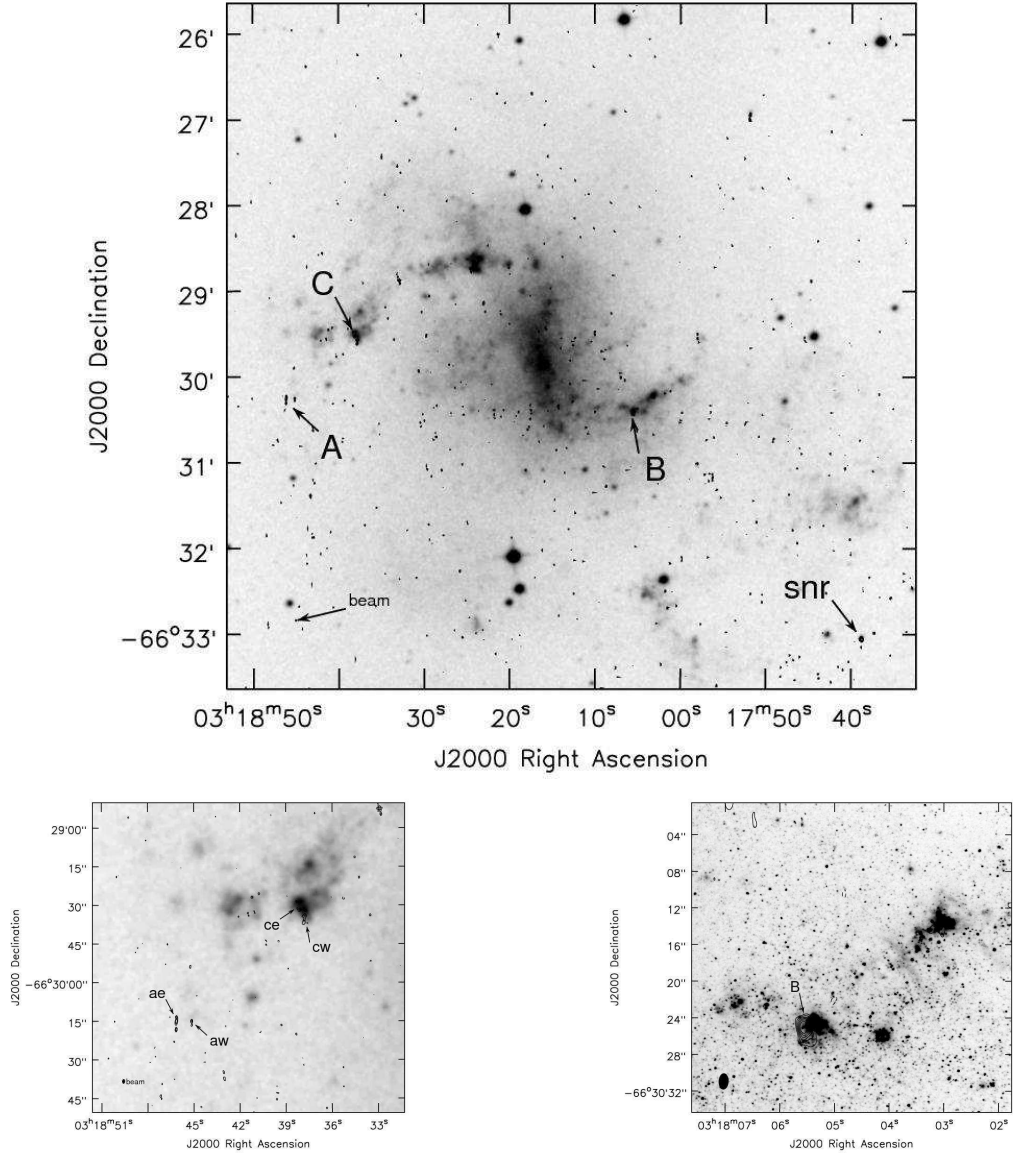
Fig. 5.— **NGC 1313**. ATCA 6.2 cm (4.8 GHz) radio contours of $-3, 3, 4, 5, 6, 7, 8, 10, 12, 14 \times \sigma$ ($54\ \mu\mathrm{Jy\ bm^{-1}}$) are overlaid on a Las Campanas Observatory (LCO) 2.5 m optical image. The star formation region NGC 1313b (n1313-341 of Larsen (2004)) is the radio-bright region on the right. SNR 1978K is also shown. The beam size (2.5×1.5 arcsec) is indicated at the lower left. Blow-ups show the components of the "A" and "B" regions.
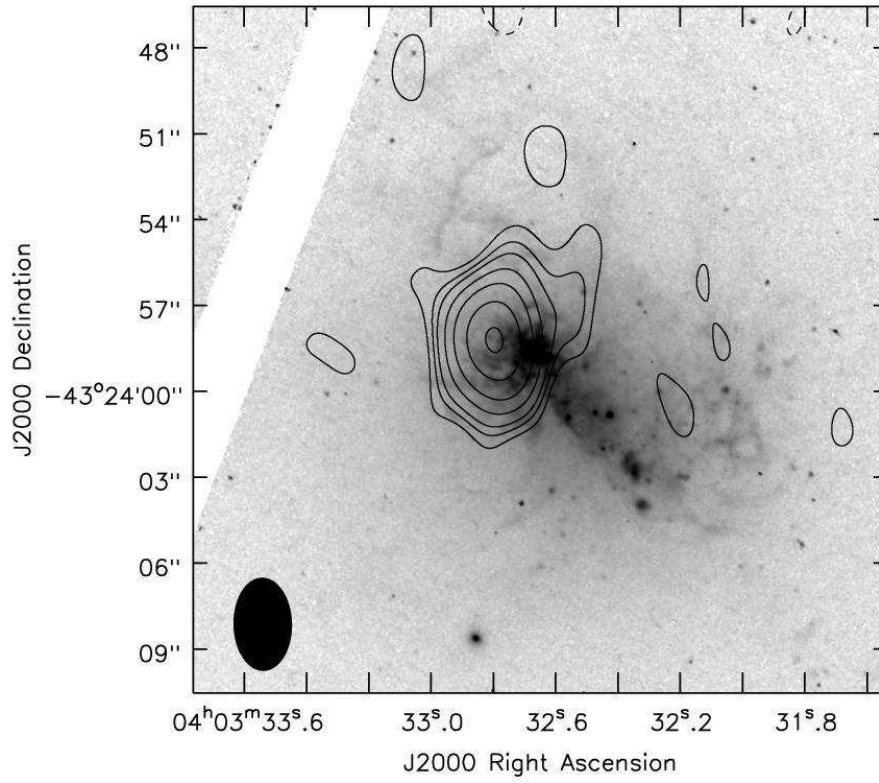
Fig. 6.— **NGC 1510**. ATCA 3.5 cm (8.5 GHz) contours of $-3, 3, 4, 5, 7, 10, 15, 21 \times \sigma$ (39 μJy bm^{-1}) are overlaid on an optical *HST* ACS F658N image. The beam size $(2.6 \times 1.7$ arcsec) is indicated at the lower left. *HST* astronomy is precise to within ~ 1 arcsec.
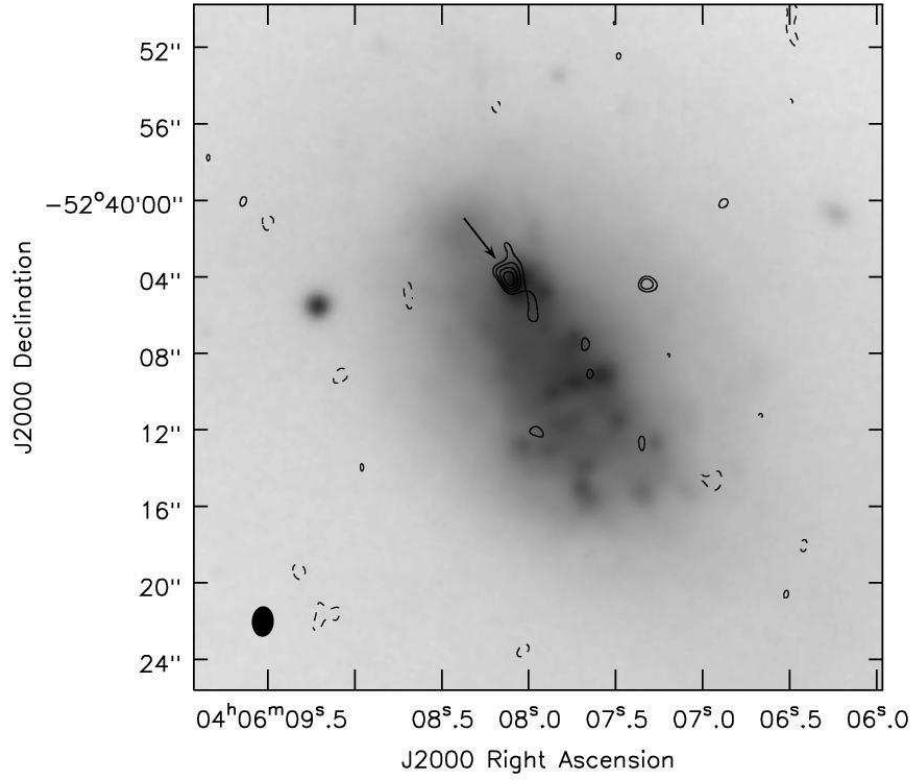
Fig. 7.— **NGC 1522**. ATCA 3.5 cm (8.5 GHz) radio contours of $-3, 3, 3.5, 4, 4.5 \times \sigma$ (39 μJy bm^{-1}) are overlaid on an optical image from the LCO 2.5 m. The beam size (2.3×1.7 arcsec) is indicated at the lower left.
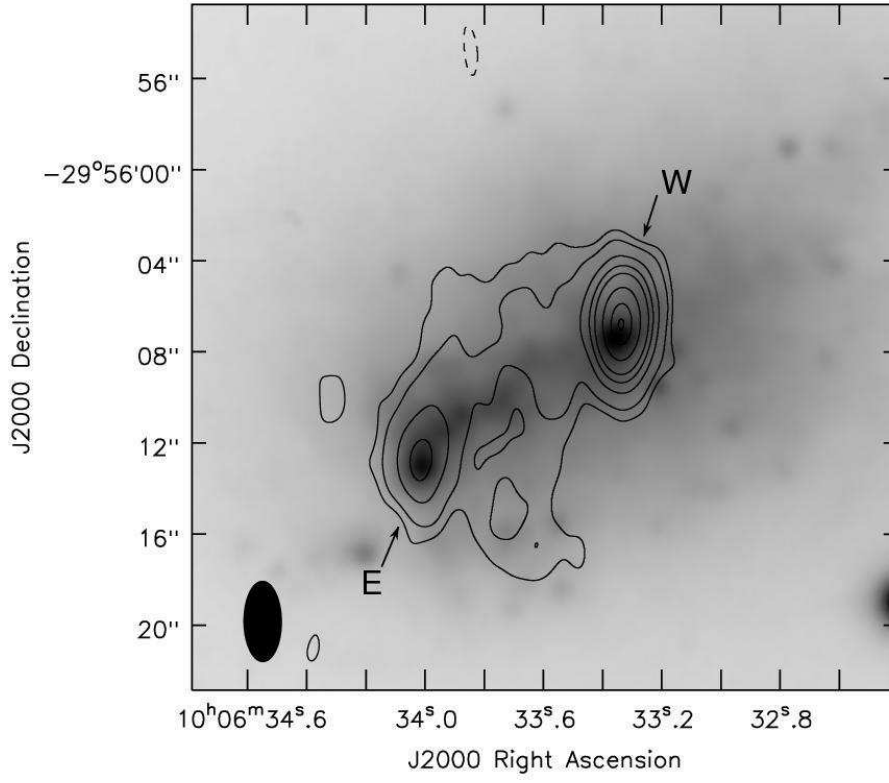
Fig. 8.— **NGC 3125**. ATCA 3.5 cm (8.5 GHz) radio contours of $-3, 3, 5, 10, 15, 20, 30, 40, 45 \times \sigma$ (53 μJy bm^{-1}) are overlaid on an LCO 660 nm optical image. The beam size (3.6×1.7 arcsec) is indicated at the lower left.
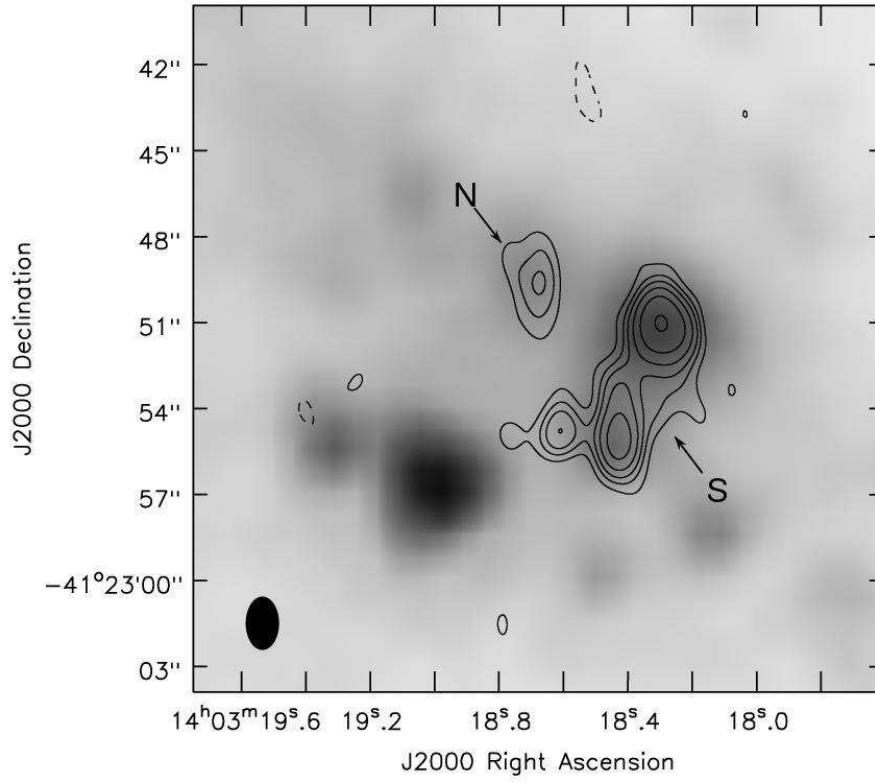
Fig. 9.— **NGC 5408**. ATCA 3.5 cm (8.5 GHz) radio contours of $-3, 3, 5, 7, 10, 15, 25 \times \sigma$ (42 μJy bm^{-1}) are overlaid on a *Spitzer* IRAC 3.6 μm infrared image from the SINGS catalog (Kennicutt et al. 2003). The beam size (2.6×1.7 arcsec) is indicated at the lower left.

Table 5.   Inferred Properties of Thermal[a] Radio Sources

Source	Size[b] (pc)	$Q_{\rm Lyc}$ Lower Limit ($\times 10^{50}$ s^{-1})	Stellar Mass ($\times 10^5 M_\odot$)	O7.5 V Stars[c] (min. number)
VLA Targets				
Arp 217a	50	130	8	1280
Arp 217b	80	110	7	1070
Arp 217e	90	300	19	2990
Arp 233n	120	470	30	4720
Arp 233s	110	730	46	7300
Mrk 35e	70	260	16	2550
Mrk 35w	60	300	18	2950
NGC 4490a	20	79	5	790
ATCA Targets				
NGC 5408n	50	7	0.4	70

Note. — Thermal sources tabulated here have spectral indices $\alpha > -0.2$.

[a]In this paper sources are considered to be predominantly thermal if $\alpha - \delta\alpha > -0.2$. Sources with $\alpha > -0.2$ but $\alpha - \delta\alpha < -0.2$ are categorized as "uncertain."

[b]This lower limit is based upon the distances in Table 6 and deconvolved angular sizes in Tables 3 and 4.

[c]Assuming O7.5 V stars have a $Q_{\rm Lyc} = 1.0 \times 10^{49}$ s^{-1} (Vacca 1994)

Table 6.   Detection Limits of Radio Sources

Source	Distance[a] (Mpc)	Cas A Limit (σ)	"Non-thermal" Sources	W49A Limit (σ)	"Thermal" Sources	Ambiguous Sources
VLA Targets						
Arp 217	14.4	0.9	1	0.5	3	1
Arp 233	20.4	0.5	⋯	0.3	2	⋯
Arp 263	9.1	2.4	⋯	1.4	⋯	⋯
Arp 266	11.9	1.3	⋯	0.7	⋯	⋯
Arp 277	11.8	1.3	⋯	0.8	⋯	⋯
Arp 291	15.4	0.8	⋯	0.5	⋯	⋯
Arp 32	17.8	0.6	⋯	0.4	⋯	⋯
Mrk 1063	20.2	0.5	⋯	0.3	6–7[b]	⋯
Mrk 1080	11.1	1.6	⋯	1.0	⋯	⋯
Mrk 1346	13.8	1.0	⋯	0.6	⋯	⋯
Mrk 1479	4.6	9.5	⋯	5.6	⋯	⋯
Mrk 35	13.8	1.0	⋯	0.6	2	⋯
Mrk 370	11.7	1.6	⋯	0.9	⋯	⋯
Mrk 829	17.5	0.7	⋯	0.4	⋯	⋯
Mrk 86	6.1	4.7	⋯	2.8	⋯	⋯
NGC 1156	6.1	4.9	⋯	2.9	⋯	⋯
NGC 3003	19.8	0.4	⋯	0.2	⋯	⋯
NGC 4490	8.4	1.2	2	0.7	2	2
ATCA Targets						
NGC 1313	4.2	5.8	2	3.4	⋯	4
NGC 1510	10.4	1.1	⋯	0.6	⋯	1
NGC 1522	10.0	1.1	1	0.6	⋯	⋯
NGC 2101	13.7	0.7	⋯	0.4	⋯	⋯
NGC 3125	12.3	0.6	⋯	0.3	⋯	2
NGC 5408	5.0	3.2	⋯	1.9	1	1
TOL 0957-278	10.4	0.7	⋯	0.4	⋯	⋯

Note. — We assume Cas A at 3.6 cm (8.5 GHz) is 612 Jy at 2.8 kpc (Baars et al. 1977), and W49A at 3.6 cm (8.5 GHz) is 57.7 Jy at 14.1 kpc (Mezger & Henderson 1967).

[a]Distances are galactocentric.

[b]Although we did not detect thermal emission from Mrk 1063, we report the number of thermal sources Hunter et al. (1994) found.